# Accepted Manuscript

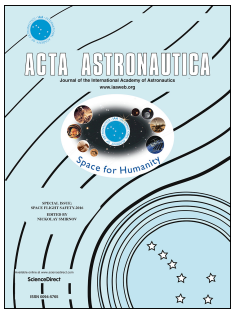


Serendipitous detection and size estimation of space debris using a survey zenith-pointing telescope

Bikram Pradhan, Paul Hickson, Jean Surdej

PII: S0094-5765(18)32127-1

DOI: https://doi.org/10.1016/j.actaastro.2019.07.008

Reference: AA 7589

To appear in: *Acta Astronautica*

Received Date: 21 December 2018

Revised Date: 6 June 2019

Accepted Date: 9 July 2019

Please cite this article as: B. Pradhan, P. Hickson, J. Surdej, Serendipitous detection and size estimation of space debris using a survey zenith-pointing telescope, *Acta Astronautica* (2019), doi: https://doi.org/10.1016/j.actaastro.2019.07.008.

# Serendipitous detection and size estimation of space debris using a survey zenith-pointing telescope

Bikram Pradhan[a], Paul Hickson[a,b], Jean Surdej[a]

[a] *Space science, Technologies and Astrophysics Research (STAR) Institute, Université de Liège, Institut d'Astrophysique et de Géophysique, Allée du 6 Août 19c, 4000 Liège, Belgium*

[b] *Department of Physics and Astronomy, The University of British Columbia, 6224 Agricultural Road, Vancouver, BC, V6T1Z1, Canada*

**Abstract**

The size distribution of space debris constitutes an important input to risk analysis for current and future space missions. In preparation for future observations with the zenith-pointing 4-m International Liquid Mirror Telescope (ILMT), the 1.3-m Devasthal Fast Optical Telescope (DFOT) was used to gain experience with zenith-pointing observations and, serendipitously, to detect, identify and characterize orbital debris. Observational data were acquired on 11 nights in May 2015 using a 2048 × 2048-pixel CCD detector operating in time-delay integration mode. Thirteen debris streaks were detected, mostly during dawn and twilight. All were identified by correlation with available two-line element sets. By modeling each of the objects as a diffuse-specular Lambertian sphere with an albedo $\rho = 0.175$, their effective diameters were estimated from the observed apparent magnitudes, altitudes, velocities and solar phase angles. Seven objects were found to be in low Earth orbits and five in mid-Earth or geo-transfer orbits. The apparent Gaia magnitudes of the identified objects range from 5.6 to 12.0 and their estimated effective diameters from 0.8 to 7.6 m. The detection size limit of DFOT is found to be 50 cm for objects orbiting at an altitude of 1000 km. Images from the future ILMT photometric survey are expected to provide detections of space debris having diameters as small as 5 cm at this altitude.

*Keywords:*

*Email addresses:* bpradhan@uliege.be (Bikram Pradhan), hickson@physics.ubc.ca (Paul Hickson), jsurdej@uliege.be (Jean Surdej)

Space debris, Optical survey, Image processing

## 1. Introduction

Orbital debris in the Earth-space environment poses a threat to the survivability of resident satellites and future space missions [1, 2]. Debris present at altitudes ranging from low-Earth orbits (LEO - an altitude of 2000 km or less) to geosynchronous orbits (GEO) consists primarily of expired spacecraft, rocket stages, separation devices and products of collision or breakup of satellites [3]. The only natural mechanism for debris removal is atmospheric drag, which is relatively slow even for objects in LEO. The larger objects can be tracked and thereby avoided. But, many smaller objects are not yet cataloged. A pragmatic approach to analyze the risk involves a better understanding of the debris population and its size distributions for different orbital regions.

Ground-based observations employ radar or reflected sunlight to detect and track orbiting objects [4, 5]. Most debris objects have near-circular orbits [6]. The orbital radius, and distance from the observer can then be determined from the observed position, angular rate, and time of observation. In an optical observation, these parameters can be determined from the length of the streak that the objects leave on timed exposures, or angular distance traveled if they appear in two or more sequential exposures. The orientation of the streak provides information on the inclination of the orbit. If one assumes an albedo and phase function, the size is readily estimated [7, 8]. Identification of the detected objects can be achieved by matching the derived ephemeris and direction of the streak with predicted values for cataloged objects.

The NASA Orbital Debris Observatory (NODO) used a fixed 3-m liquid metal (mercury) mirror telescope (NASA-LMT) [9] and a 32-cm Schmidt telescope (CDT) [10] for optical detection of orbital debris. A new facility, the International Liquid Mirror Telescope (ILMT) [11, 12] is expected to achieve first light this year. While its primary purpose is to conduct astronomical surveys, the data that will be obtained will have many uses, including the detection and characterization of orbital debris. The ILMT will implement a 4-m liquid mirror coupled to a wide-field optical CCD camera employing time-delay-integration readout (TDI). Borra et al.[13, 14] have first suggested to use a CCD in TDI mode sky observations with liquid mirrors. The ILMT

always points towards the zenith due to constraints on its mechanical stability. At the same time, the readout rate of each row of the CCD image is synchronized to the angular speed of the sky passing overhead. This whole setup provides the advantage of always working under the best seeing conditions as it encounters the least air-mass (Z=1). Scanning the same part of the sky repeatedly by the fixed telescope also enables one to access fainter sources by co-adding CCD frames of the same field and to detect variable or moving objects by subtraction of CCD frames acquired on different nights.

In preparation for the ILMT survey, we have obtained and analyzed several nights of data using a conventional optical telescope in observations at the zenith, using a CCD image sensor operating in TDI mode. The telescope employed was the 1.3-m Devasthal Fast Optical Telescope (DFOT) of the Aryabhatta Research Institute of Observational Sciences (ARIES, Uttarakhand, India) [15]. This telescope is located adjacent to the ILMT, at N29°21′42″ E79°41′06″ and 2410-m altitude, and therefore experiences very similar observing conditions. Here, we describe our data analysis techniques and present results for the detected objects.

## 2. Data Acquisition and Reduction

Observations were conducted by parking the telescope near the zenith and implementing TDI mode, also known as drift-scanning, to compensate for the Earth's rotation [16, 17]. This is the observing mode that will be used for the ILMT. The detector used was an SBIG 2K × 2K CCD camera, having a field of view of 10.1×10.1 arcmin and an image scale of 0.295 arcsec per pixel. The gain of the CCD was 0.72 $e^-$/ADU and its readout noise was approximately 15 $e^-$. Three filters were employed, matching the g′, r′ and i′ wavelength bands of the Sloan Digital Sky Survey (SDSS) [18]. One of these filters was inserted at the beginning of each night and used for the entire night. The median seeing (FWHM) was found to be 1.1 arcsec. In TDI mode, the CCD is read continuously. The effective integration time for celestial objects is the time required for their images to drift across the length of the CCD, which in our case was 46.1 seconds. In practice, the length of the acquired CCD frames was limited by the memory available to the data acquisition system. As a result, each recorded frame has a dimension of $\mathbf{27952 \times 2048}$ pixels, corresponding to a $\mathbf{2.29^\circ \times 10.1'}$ field of view. The temperature of the CCD was maintained close to $-27^\circ$ C by means of a Peltier cooling system.

Observations were made during 11 nights in May, 2015 (see Table 1). However, approximately 60% of the observing time was lost due to bad weather (pre-monsoon season). Of course, orbital debris can be detected optically only when illuminated by the Sun. Particularly, LEO objects can be observed only within a few hours from sunset and sunrise.

### *2.1. Preprocessing*

TDI data present some unique aspects compared to framed images. Each row of the image is read out at a different time, so any temporal variations in CCD temperature will result in a systematic variation of dark current in the scan direction (right ascension). Similarly, changes in sky brightness will produce background variations in the images.

In our case, a gradient in dark current was observed, primarily in the orthogonal (declination) direction. This was removed by subtracting a 1-dimensional mean dark from each row of the image. This mean dark was computed by taking the mean of all rows in several dark frames, using a one-time rejection of outliers that differ by more than 1.5 standard deviations ($\sigma$) from the mean.

In TDI images, the output signal is proportional to the sum of the charges generated by the individual pixels in the scan direction. Effectively, the detector response function is averaged along the scan direction. The result is a very uniform response that varies only in the orthogonal direction. These small residual sensitivity variations were corrected by creating a normalized 1-dimensional flat-field from background sky light. After dark subtraction, the average of the pixel values was taken along the scan direction, again using 1.5-$\sigma$ outlier rejection. The resulting 1-dimensional sensitivity map was normalized and then applied to (divided into) every row in the science images.

Sky subtraction was performed by fitting each image, after dark and flat-field correction, with a smooth two-dimensional polynomial, using outlier rejection to remove the stars. This polynomial was then subtracted in order to remove the sky. The effectiveness of these preprocessing steps is illustrated in Figure 1.

### *2.2. Astrometric and Photometric calibration*

The Sextractor algorithm [19] was used to build a catalog of objects present on each individual preprocessed image. A threshold intensity of

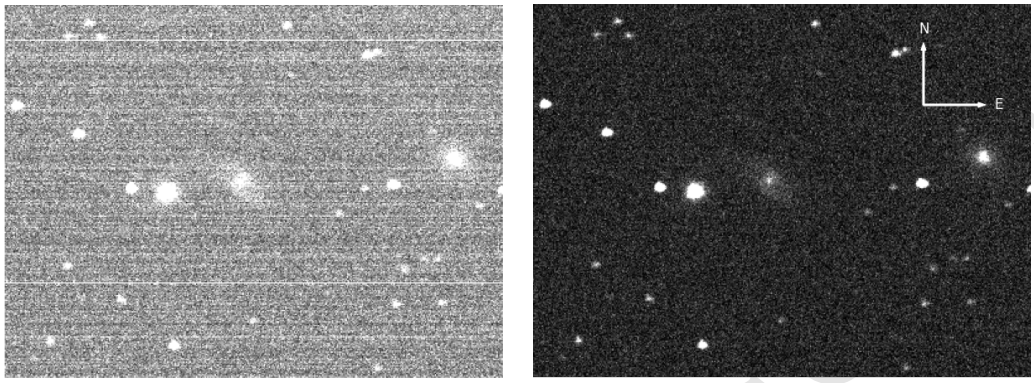


Figure 1: Comparison of a subimage before (left) and after preprocessing (right). An area of $\mathbf{4}' \times \mathbf{3.5}'$, centered at $18^h02^m{+}29^\circ$ (J2000.0), is shown. The image was taken on 24 May 2015 at 20:34:46 UTC, using the SDSS g′ filter.

1.5-$\sigma$ above the local background, determined from the median of a $64 \times 64$-pixel surrounding region, was applied to isolate connected groups of pixels (objects). A minimum object area of 10 pixels was considered. For each detected object, the centroid was computed by modelling it with a Gaussian ellipsoidal intensity distribution. This resulted in instrumental magnitudes and centroid positions for all detected objects.

Calibrated magnitudes of the detected sources were obtained by matching detected stellar objects with stars in the Gaia Data Release 1 catalog [20, 21]. The published Gaia magnitudes ($m_G$) were used to estimate the zero-point offset between calibrated magnitudes and our instrumental magnitudes. Astrometric calibration was performed by applying corrections for nutation and aberration to the instrumental positions, and then precessing the resulting coordinates to a standard epoch, J2000. These were then compared to the corresponding Gaia positions. Coefficients of a bilinear transformation between instrumental and calibrated positions were determined by minimizing the squared residuals for the matched stars. To improve the calibration in both photometry and astrometry, very faint objects having $m_G > 17$ were excluded. Depending on the galactic latitude of the fields, typically one to two hundred stars were available for the calibration of each image.

The resulting RMS astrometric precision was found to be 0.1 arcsec in declination and 0.15 arcsec in right ascension, as seen in Figures 2 and 3. The RMS photometric precision is 0.04 magnitude (refer to Figure 4). This

degree of photometric error is not unexpected due to the differences between the SDSS wavelength bands and the broad-spectrum Gaia response.

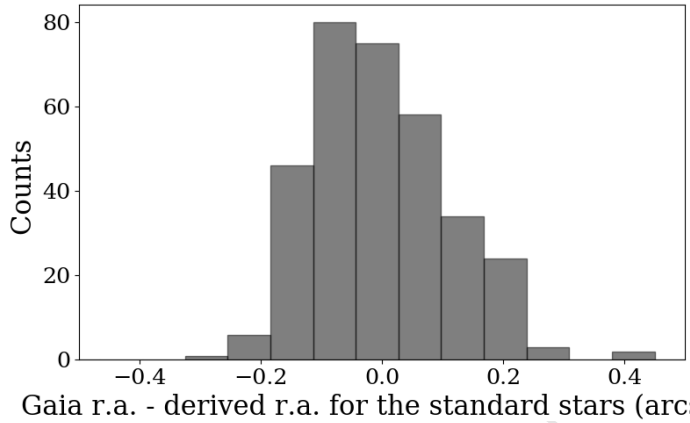


Figure 2: Histogram of the residuals in right ascension **(r.a.)** after astrometric calibration with stars from the Gaia catalog. This is for a single field image, obtained on 19 May 2015 at 21:04:17 UTC, within $18^h12^m - 18^h23^m$ ra range (2015.4 epoch) using the SDSS g′ filter.

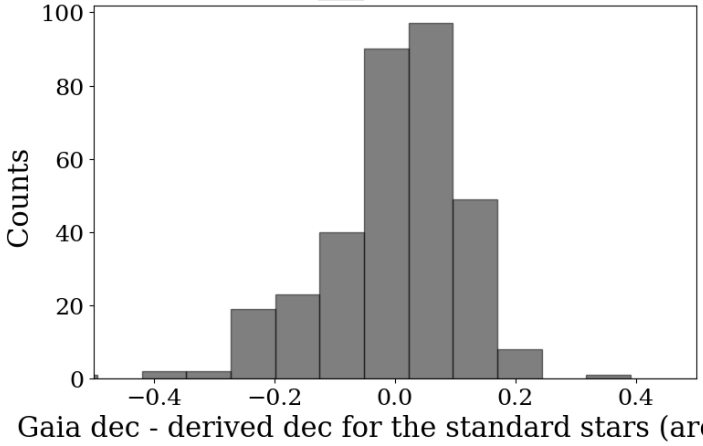


Figure 3: Histogram of the residuals in declination **(dec)** after astrometric calibration with stars from the Gaia catalog. This is for a single field image, obtained on 19 May 2015 at 21:04:17 UTC, in the r.a. range of $18^h12^m - 18^h23^m$ (2015.4 epoch) using the SDSS g′ filter.

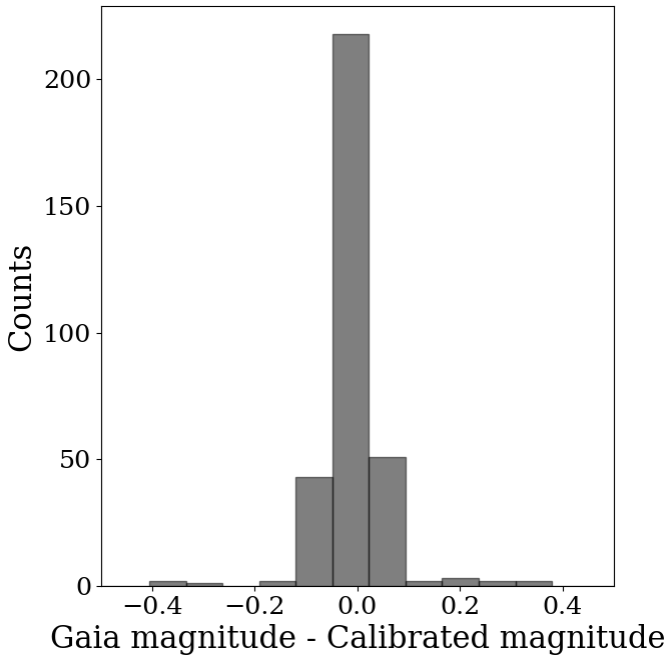


Figure 4: Histogram of the residuals obtained by subtracting the Gaia magnitudes of the detected standard sources from those derived in the present work. This is the result obtained after calibrating a single data block, obtained on 19 May 2015 at 21:04:17 UTC, in the r.a. range of $18^h12^m - 18^h23^m$ (2015.4 epoch) using the g′ SDSS filter.

## 3. Debris detection and identification

Thirteen linear debris streaks were visually identified in the processed images. These are illustrated in Figure 5. To determine the position and flux of each, a line was fit connecting the endpoints of the streak. For each column, pixels within a distance of ±4 times the stellar FWHM of this line were used to generate a profile, with 0.1-pixel resolution, by cubic spline interpolation. The profiles for each column were then shifted and co-added, using cross correlation to determine the required shifts. This resulted in a low-noise composite profile of the line in the scan (r.a.) direction. This profile was then fit to each individual column of data, using least squares analysis to determine the best amplitude and shift. The uncertainty in estimating the positions of bright streaks on the CCD images was found to be less than a pixel, whereas in fainter streaks the uncertainty increased up to 10 pixels. The fitted profile was then integrated to estimate the total flux in the streak

for each column of the image. From this, a one-to-one relationship between flux and position along the streak was obtained. For some objects, this was converted to a light curve (flux vs time) using the angular rate predicted for the object based on its identification (described below).

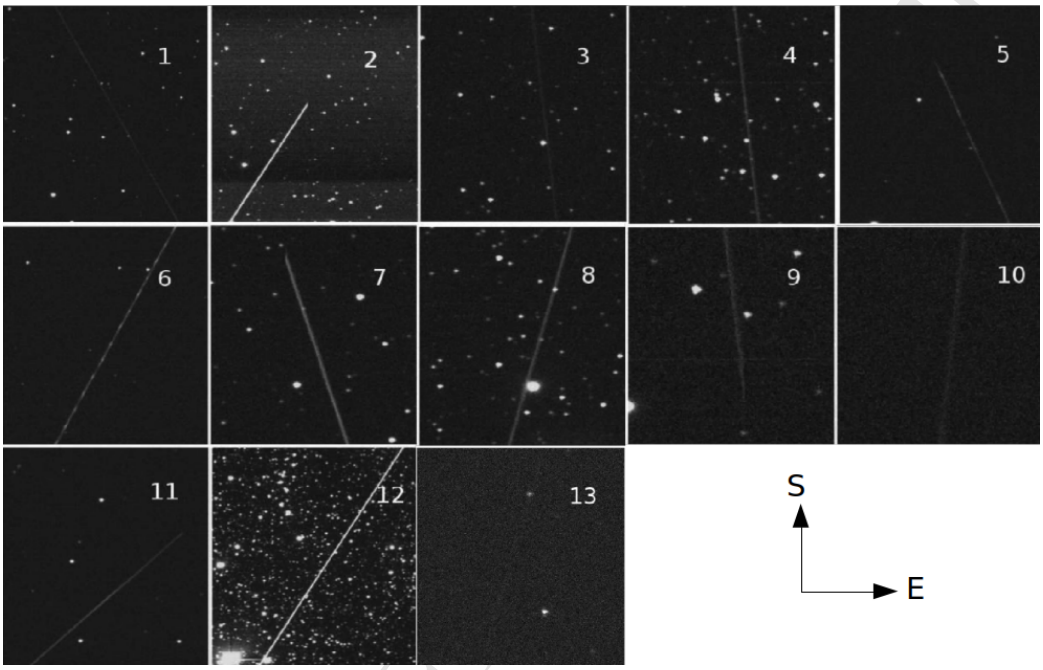


Figure 5: Images of the 12 detected objects passing through the CCD field of view. Images 2 and 12 show the same object, detected on two different nights. All the images of the collage are cropped for a better visualization.

Some objects showed quasi-periodic photometric variations (e.g. Figure 6) in their light curves (e.g. object 6 in Figure 5). This is very likely due to the object rotating, causing sunlight to be reflected in a recurrent manner. By analyzing such light variations, one can set interesting constraints on the shape of the object. However, such an analysis is beyond the scope of this research paper.

The direction of each object, i.e., the angle $\phi$ subtended by the streak from North towards East was measured from the images. Although the telescope is not tracking and the Earth is rotating, the TDI scan removes this rotation, so the direction measured on a TDI image is the actual direction of the object in the International Celestial Reference System (ICRS) inertial frame.

With TDI observations, the time at which the object crosses the detector is generally uncertain, because the exact position at which it crossed the CCD is not known. For our observations, images of celestial objects move across the CCD in ∼46 seconds, which is the time required to move charges from one side of the CCD to the other. So the time of detection of a moving object is uncertain by as much as 23 seconds, depending on where it crossed the detector. An exception to this occurs if the object enters or leaves the CCD at an edge that is perpendicular to the scan direction. In that case, the streak ends abruptly, as can be seen for objects 2, 5, 7, 9 and 11 in Figure 5. From the direction of the streak and making use of the TLE (see below), one can determine whether the object entered or exited at the edge where the charges are read out. Thus the time of entry or exit is known within the precision of the read-out time of the corresponding CCD pixel row. The precision was found to be ±1 second considering the accuracy of the synchronization between the computer's clock and its online time source.

A set of python programs written by one of us (PH) was used to correlate the observed streaks with cataloged objects having two line elements (TLE) generated on the same observing date available from the U.S. Air Force Space Command [22]. Each TLE was propagated using the SGP4/SDP4 algorithm [23, 24] and used to predict topocentric positions of the objects as seen from the DFOT observatory, as well as their altitude, angular velocity and direction. Objects predicted to pass through the field of view of the telescope during the observing period, while at the same time being illuminated by the Sun, were selected. By comparing the observed time and direction of the streak with those predicted from the TLE database, all of the 13 detections were identified. One object (SSN 24827; objects 2 and 12 in Figure 5) was detected on two different nights. The predicted and observed parameters for these objects are listed in Table 2.

## 4. Size estimation

The shape and surface structure of orbital debris can be very complex. So, it is difficult to describe accurately a vast population of debris with a unique model. From the satellite catalog information available from the U.S. Air Force Space Command, 8 out of the 12 identified objects are found to be non-functional payloads and the others are rocket bodies. A study conducted by Hejduk [25] suggests that the photometric behavior of 50% of non-geostationary payloads, 70% of rocket bodies and 80% of debris objects

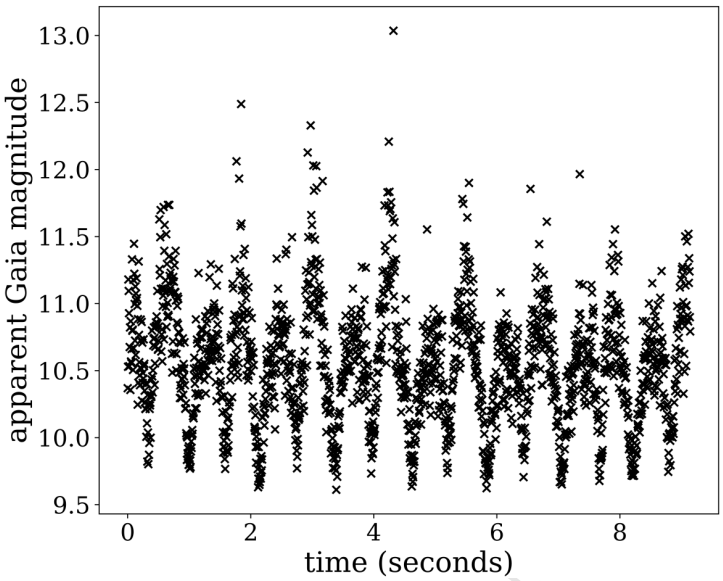


Figure 6: The light curve of object 6, detected on 18th May 2015, showing periodic variations with two distinct maxima and minima, probably due to rotation of an irregular body. The angular velocity of this object is approximately 1 rotation per second.

can be represented by a diffuse-specular Lambertian sphere model. Based upon this model, the diameter $d$ of the sphere is related to its apparent magnitude $m$, solar phase angle $\varphi$, range $r$ and albedo $\rho$ as,

$$d = \frac{r10^{-0.2(m-m_{\odot})}}{\sqrt{\rho[\frac{\beta}{6\pi}[\sin\varphi + (\pi-\varphi)\cos\varphi] + \frac{1-\beta}{16}]}}, \tag{1}$$

where $\beta$ is a mixing coefficient (refer to Appendix A for a complete derivation of the above formula). This means that a value of $\beta = 1$ or 0 would represent a purely diffused or specular sphere, respectively. In this analysis equal weight to both the specular and diffuse components were assigned by setting $\beta$ at 0.5. For comparison, we also considered the case $\beta = 1$ (pure diffuse Lambertian sphere) (see Table 2). Hejduk [25] also demonstrated that contribution of earthshine on the size estimation for objects having small solar phase angle ( $\varphi < 120°$) is negligible. As the objects listed in Table 2 have smaller $\varphi$, we did not have to take into account the effect of earthshine in our analysis.

To estimate the apparent magnitude $m_G$ of the object, the total flux $f$ of

the streak was divided by the time taken to cross the detector, which is the ratio between the angular streak length $l$ and the angular rate $v$ computed from the TLE,

$$m_G = -2.5 \log(fv/l) + m_0, \tag{2}$$

where $m_0$ is the magnitude zero point determined by matching stars in the Gaia catalog.

The apparent Gaia magnitude of the Sun was estimated by applying the color transformation given by Jordi et al. [26] to the Sun's V magnitude of $-26.72$. This leads to $m_{G\odot} = -26.95 \pm 0.38$.

The albedo $\rho$ was taken to be 0.175 [8]. Since our observations were made near the zenith, the range is equal to the altitude of the object, which was determined from the TLE. The solar phase angle was computed from the observation time and observatory topocentric coordinates using standard relations. The estimated diameters of the detected objects are listed in Table 2. The uncertainties in the size estimation were calculated from the uncertainties found in the flux estimation.

From the ESA's Database and Information System Characterising Objects in Space (DISCOS) [27, 28], the estimated cross-section of 10 of the 12 identified debris could be retrieved. This database contains the minimum and maximum observed cross-section of the resident space objects. We also calculated the optical cross-section ($\pi d^2/4$) for those 10 objects from the current diameter $d$ (see Table 2). These independent sets of results are presented in Table 3. The size estimates for both the hybrid model and pure diffuse Lambertian sphere model are found to be comparable to the measurements obtained from the online source except for the case of object 4. We also could obtain the shape and size information of object 2 (SSN 24827) from Zak [29]. The object was found to be a reconnaissance satellite equipped with a telescope setup of 2 meters diameter and a length of 6.9 meters. There are also solar panels attached to it. So, the dimensions of the satellite can possibly come in agreement with our effective optical diameter estimates of 7.6 or 5.9 meters listed in Table 2.

The limiting magnitude for 1000-km LEO objects seen at a solar phase angle of 50° with a $\beta$ value of 0.5, is estimated from the faintest observed track, which has a signal-to-noise ratio of 18, to be $m_G \simeq 8.4$ for the DFOT telescope under seeing conditions of 1 arcsec. This corresponds to a diameter of 50 cm. The signal-to-noise ratio of the streak was calculated by dividing the total integrated flux from the streak by the total noise from an equivalent

streak area. Under similar conditions, the larger aperture and field of view of the ILMT with a better telescope system efficiency (see Table 5) should result in a limiting magnitude of $m_G \simeq 13.6$, with a corresponding diameter of 5 cm. **Considering a signal-to-noise ratio similar to the faintest track observed with DFOT, the flux of the faintest object recognizable on the ILMT CCD detector was predicted using the ILMT telescope system parameters given in Table 5 and subsequently the corresponding limiting magnitude was calculated using the aforementioned observing conditions.** A comparison of diameter limits for both telescopes, as a function of altitude, is shown in Figure 7. Considering the 11 allocated nights of observation and the two-line element predictions, we found that 10 additional cataloged objects passed the field of view of the 1.3-m DFOT at the appropriate times but these were not detected on our frames. So, the limiting magnitude is used to set a maximum size limit ($d_{max}$) to these objects. However, the size information on these objects could not be found from online sources for a comparison. The list of all undetected objects and the maximum size limit assigned to them are listed in Table 4.

An automatic detection algorithm with a high sensitivity for detecting fainter streaks should be implemented in order to detect smaller debris. This will strengthen the statistics on the fainter debris population and their sizes. Such an approach, its efficiency and outcomes will be presented in another paper.

## 5. Conclusions

Optical observation of space debris constitutes an important asset, providing statistics on the number densities and sizes present at different altitudes. Zenith-pointing telescopes such as the ILMT can make a contribution in this area. Operating in TDI mode, observations will be carried out in survey mode and will be sensitive to any objects passing through the field of view.

In this test study, the 1.3-m DFOT telescope was operated in the same TDI mode as that of the ILMT. The efficient data reduction technique applicable to the TDI frames provided a photometric precision of 0.04 magnitudes and astrometric precision of approximately 0.1 arcsec for point like objects. 12 objects were successfully detected passing overhead in the form of streaks on the CCD images. Identification of the objects was achieved by cross matching their observed time and direction to those from the TLE. Once the identifications were made, their apparent magnitudes were derived using

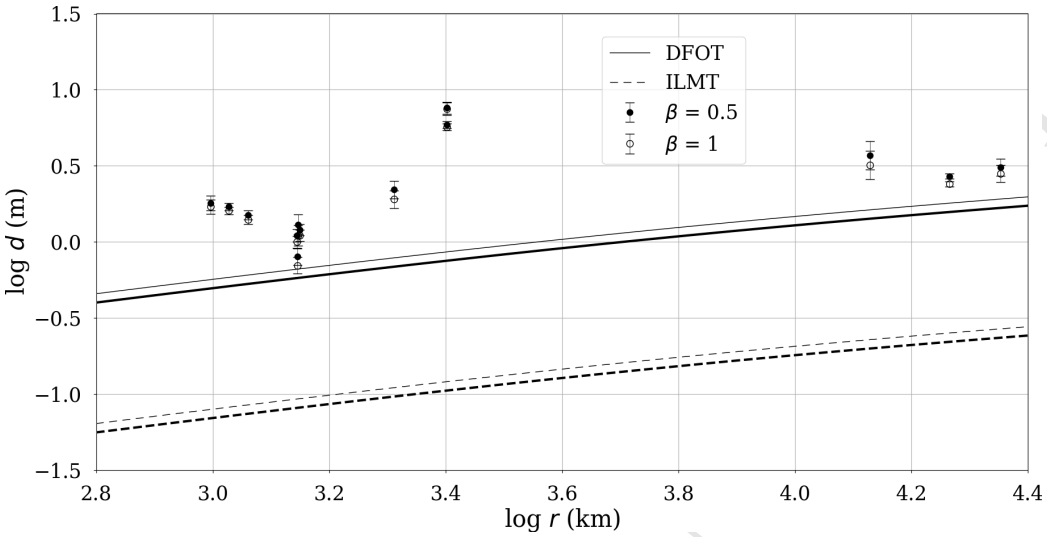


Figure 7: Estimated size of the identified debris as detected by DFOT for the $\beta$ values of 1 (thick lines) and 0.5 (thin lines). The solid lines indicate the minimum detection capability of DFOT. The dashed lines indicate the predicted detection threshold for the ILMT.

TLE information on their angular velocity and altitude. The time resolution of these photometric measurements depend on the velocity and the orientation of the streak. The error associated with the derived magnitudes of the objects are calculated from the noise present in the streak signal. It is to be noted that, adopting this procedure, the optical magnitude of the detected objects can not be determined unless they are identified. **Hence, it will be difficult to characterize uncatalogued detected objects since no prior information on their angular velocity and altitude is available.** The precision of the detection time of the objects was found to vary between 1 and 23 seconds. However, the uncertainties associated with TLE predictions may also lead to some faulty identification of the objects.

If the hybrid diffuse-specular Lambertian sphere is representative of this population of space debris, their estimated diameters range from 0.8 to 7.6 m. Cross-section estimates of 9 out of the 10 identified objects are consistent with the values retrieved from online sources, while one (object 4) seems to differ appreciably. Compatibility of the size estimates can be better addressed in the future thanks to multiple detection of the objects with a dedicated telescope, such as ILMT.

The detection threshold of DFOT could be used to set an upper size limit to fainter debris which have crossed the field of view of the DFOT CCD but were not visually detected.

The 4-m ILMT telescope, with its 22-arcmin-square field of view and fainter detection threshold, should be able to detect many more space debris, down to a size of approximately 5 cm in low Earth orbits.

## Acknowledgements

We extend our gratitude to Wallonie - Bruxelles International (WBI) (www.wbi.be) for funding this research. We also thank the ARIES observing staff and technical assistants for their support during the observing run. PH acknowledges financial support from the Natural Sciences and Engineering Research Council of Canada and the F.R.S. - F.N.R.S. during a sabbatical leave in 2018 at Liège University, Belgium. This work has made use of data from the European Space Agency (ESA) mission *Gaia* (https://www.cosmos.esa.int/gaia), processed by the *Gaia* Data Processing and Analysis Consortium (DPAC, https://www.cosmos.esa.int/web/gaia/-dpac/consortium). Funding for the DPAC was provided by national institutions, in particular the institutions participating in the *Gaia* Multilateral Agreement. We also thank Dr. Brajesh Kumar and Shashank Shekhar for their assistance during the observations.

## References

[1] B. Zhang, Z. Wang, Y. Zhang, Collision risk investigation for an operational spacecraft caused by space debris, Cambridge, UK: Cambridge University Press, 2017. doi:10.1007/s10509-017-3041-z.

[2] H. Schaub, L. E. Z. Jasper, P. V. Anderson, D. S. McKnight, Cost and risk assessment for spacecraft operation decisions caused by the space debris environment, Acta Astronautica 113 (2015) 66–79. doi:10.1016/j.actaastro.2015.03.028.

[3] V. A. Chobotov, D. E. Herman, C. G. Johnson, Collision and debris hazard assessment for a low-Earth-orbit space constellation, Journal of Spacecraft and Rockets 34 (1997) 233–238. doi:10.2514/2.3198.

[4] D. Mehrholz, F. W. Leushacke, R. Jehn, H. Klinkrad, M. Landgraf, Detecting, tracking and imaging space debris, ESA Bulletin 109 (2002) 128–134.

[5] S. Lederer, H. Cowardin, B. Buckalew, J. Frith, P. Hickson, L. Pace, M. Matney, P. Anz-Meador, P. Seitzer, E. Stansbery, T. Glesne, NASA's Orbital Debris Optical and IR Ground-based Observing Program: Utilizing the MCAT, UKIRT, and Magellan Telescopes, in: Advanced Maui Optical and Space Surveillance Technologies Conference, 2016, p. 12.

[6] X. Xu, Y. Xiong, A method for calculating collision probability between space objects, Research in Astronomy and Astrophysics 14. doi:10.1088/1674-4527/14/5/009.

[7] M. Mulrooney, M. Matney, Derivation and Application of a Global Albedo Yielding an Optical Brightness to Physical Size Transformation Free of Systematic Errors, in: Advanced Maui Optical and Space Surveillance Technologies Conference, 2007, p. E81.

[8] M. Mulrooney, M. Matney, A New Bond Albedo for Performing Orbital Debris Brightness to Size Transformations, in: 59th International Astronautical Congress, 2008, p. Paper ID: 343.

[9] A. E. Potter, M. Mulrooney, Liquid metal mirror for optical measurements of orbital debris, Advances in Space Research 19 (1997) 213–219. doi:10.1016/S0273-1177(97)00003-3.

[10] T. Schildknecht, M. Ploner, U. Hugentobler, The search for debris in GEO, Advances in Space Research 28 (2001) 1291–1299. doi:10.1016/S0273-1177(01)00399-4.

[11] J. Surdej, O. Absil, P. Bartczak, E. Borra, J.-P. Chisogne, J.-F. Claeskens, B. Collin, M. De Becker, D. Defrère, S. Denis, C. Flebus, O. Garcet, P. Gloesener, C. Jean, P. Lampens, C. Libbrecht, A. Magette, J. Manfroid, D. Mawet, T. Nakos, N. Ninane, J. Poels, A. Pospieszalska, P. Riaud, P.-G. Sprimont, J.-P. Swings, The 4m international liquid mirror telescope (ILMT), in: Society of Photo-Optical Instrumentation Engineers (SPIE) Conference Series, Vol. 6267, 2006, p. 626704. doi:10.1117/12.671695.

[12] J. Surdej, P. Hickson, J.-P. Swings, S. Habraken, T. Akunov, P. Bartczak, H. Chand, M. Becker, L. Delchambre, F. Finet, B. Kumar, A. Pandey, A. Pospieszalska, B. Pradhan, R. Sagar, O. Wertz, P. Cat, S. Denis, V. J.D., J. M.K., L. P., N. N., J.-M. Tortolani, The 4-m International Liquid Mirror Telescope, Bulletin de la Société Royale des Sciences de Liège 87 (2018) 68–79.

[13] E. F. Borra, M. Beauchemin, R. Lalande, Liquid mirror telescopes - Observations with a 1 meter diameter prototype and scaling-up considerations, The Astrophysical Journal 297 (1985) 846–851. doi:10.1086/163581.

[14] E. F. Borra, R. Content, L. Girard, S. Szapiel, L. M. Tremblay, E. Boily, Liquid mirrors - Optical shop tests and contributions to the technology, The Astrophysical Journal 393 (1992) 829–847. doi:10.1086/171550.

[15] R. Sagar, B. Kumar, A. Omar, Optical Astronomical Facilities at Nainital, India, ArXiv e-printsarXiv:1304.0235.

[16] J. T. McGraw, J. R. P. Angel, T. A. Sargent, A charge-coupled device /CCD/ transit-telescope survey for galactic and extragalactic variability and polarization, in: D. A. Elliott (Ed.), Conference on Applications of Digital Image Processing to Astronomy, Vol. 264 of Proc. Society of Photo-Optical Instrumentation Engineers (SPIE), 1980, pp. 20–28. doi:10.1117/12.959777.

[17] J. F. Wright, C. D. Mackay, The Cambridge Charge-Coupled Device / CCD / System, in: Society of Photo-Optical Instrumentation Engineers (SPIE) Conference Series, Vol. 290 of Proc. Society of Photo-Optical Instrumentation Engineers (SPIE), 1981, p. 160. doi:10.1117/12.965855.

[18] J. E. Gunn, M. Carr, C. Rockosi, M. Sekiguchi, K. Berry, B. Elms, E. de Haas, Ž. Ivezić, G. Knapp, R. Lupton, G. Pauls, R. Simcoe, R. Hirsch, D. Sanford, S. Wang, D. York, F. Harris, J. Annis, L. Bartozek, W. Boroski, J. Bakken, M. Haldeman, S. Kent, S. Holm, D. Holmgren, D. Petravick, A. Prosapio, R. Rechenmacher, M. Doi, M. Fukugita, K. Shimasaku, N. Okada, C. Hull, W. Siegmund, E. Mannery, M. Blouke, D. Heidtman, D. Schneider, R. Lucinio, J. Brinkman, The Sloan Digital Sky Survey Photometric Camera, Astronomical Journal 116 (1998) 3040–3081. doi:10.1086/300645.

[19] E. Bertin, S. Arnouts, SExtractor: Software for source extraction., Astronomy and Astrophysics Supplement 117 (1996) 393–404. doi:10.1051/aas:1996164.

[20] Gaia Collaboration, A. G. A. Brown, A. Vallenari, T. Prusti, J. H. J. de Bruijne, F. Mignard, R. Drimmel, C. Babusiaux, C. A. L. Bailer-Jones, U. Bastian, et al., Gaia Data Release 1. Summary of the astrometric, photometric, and survey properties, Astronomy and Astrophysics 595 (2016) A2. doi:10.1051/0004-6361/201629512.

[21] Gaia Collaboration, T. Prusti, J. H. J. de Bruijne, A. G. A. Brown, A. Vallenari, C. Babusiaux, C. A. L. Bailer-Jones, U. Bastian, M. Biermann, D. W. Evans, et al., The Gaia mission, Astronomy and Astrophysics 595 (2016) A1. doi:10.1051/0004-6361/201629272.

[22] U.S. Air Force Space Command, space situational awareness information, `https://www.space-track.org/`, accessed: 19 December 2018.

[23] F. R. Hoots, R. L. Roehrich, Spacetrack Report #3: Models for Propagation of the NORAD Element Sets., U.S. Air Force Aerospace Defence Command, Colorado Springs, CO., 1980.

[24] D. A. Vallado, P. Crawford, R. Hujsak, T. S. Kelso, Revisiting Spacetrack Report #3, in: American Institute of Aeronautics and Astronautics, Vol. 2006-6753, 2006, pp. 1–88.

[25] M. Hejduk, Specular and Diffuse Components in Spherical Satellite Photometric Modeling, in: Advanced Maui Optical and Space Surveillance Technologies Conference, 2011, p. E15.

[26] C. Jordi, M. Gebran, J. M. Carrasco, J. de Bruijne, H. Voss, C. Fabricius, J. Knude, A. Vallenari, R. Kohley, A. Mora, Gaia broad band photometry, Astronomy and Astrophysics 523 (2010) A48. doi:10.1051/0004-6361/201015441.

[27] DISCOS (Database and Information System Characterising Objects in Space), reference for launch information, object registration details, launch vehicle descriptions, as well as spacecraft information, `https://discosweb.esoc.esa.int/`, accessed: 19 December 2018.

[28] T. Flohrer, S. Lemmens, B. Bastida Virgili, H. Krag, H. Klinkrad, E. Parrilla, N. Sanchez, J. Oliveira, F. Pina, DISCOS- Current Status and Future Developments, in: 6th European Conference on Space Debris, Vol. 723 of ESA Special Publication, 2013, p. 38.

[29] A. Zak, RussianSpaceWeb.com, news and history of astronautics in the former ussr, http://www.russianspaceweb.com/araks.html, accessed: 19 December 2018.

[30] B. Kumar, J. Shreekar, Technical parameters of the 1.3m devasthal optical telescope observatory, https://www.aries.res.in/ 1.3m/telSpecs-ver4.pdf, accessed: 19 December 2018.

[31] I. Santa Barbara Instrument Group, Operating manual research camera models: Stl-1001e, stl-1301e, stl-4020m, stl-6303e and stl-11000m, http://diffractionlimited.com/wp-content/uploads/2016/03/ST-L-Operating-Manual.pdf.

[32] B. Kumar, K. L. Pandey, S. B. Pandey, P. Hickson, E. F. Borra, G. C. Anupama, J. Surdej, The zenithal 4-m International Liquid Mirror Telescope: a unique facility for supernova studies, Monthly Notices of the Royal Astronomical Society 476 (2018) 2075–2085. arXiv:1802.00198, doi:10.1093/mnras/sty298.

[33] J. Williams, M. G.A., An analysis of satellite optical characteristics data, Planetary and Space Science 14 (9) (1966) 839 – 847. doi:10.1016/0032-0633(66)90090-0.

Table 1: Log of TDI observations†

| Date (YYYYMMDD) | Filter (SDSS) | Observation duration (UT) | Number of science images |
|---|---|---|---|
| 20150516 | i′ | $18^h01^m35^s$ to $21^h01^h32^h$ | 26 |
| | | $21^h14^m03^s$ to $23^h14^m01^s$ | |
| 20150517 | i′ | $15^h41^m14^s$ to $22^h24^m25^s$ | 33 |
| 20150518 | g′ | $14^h46^m44^s$ to $23^h08^m23^s$ | 41 |
| 20150519 | r′ | $18^h28^m00^s$ to $23^h04^m30^s$ | 23 |
| 20150520 | r′ | $16^h09^m36^s$ to $16^h20^m53^s$ | 26 |
| | | $17^h12^m38^s$ to $18^h47^m16^s$ | |
| | | $19^h00^m01^s$ to $22^h25^m07^s$ | |
| 20150521 | i′ | $17^h20^m19^s$ to $23^h09^m32^s$ | 22 |
| 20150522 | i′ | $17^h16^m34^s$ to $23^h06^m01^s$ | 23 |
| 20150523 | r′ | $14^h51^m57^s$ to $16^h43^m54^s$ | 09 |
| 20150524 | r′ | $15^h26^m38^s$ to $23^h07^m54^s$ | 38 |
| 20150525 | i′ | $15^h18^m47^s$ to $15^h30^m04^s$ | 04 |
| | | $15^h48^m09^s$ to $16^h12^m45^s$ | |
| 20150526 | i′ | $17^h59^m35^s$ to $20^h48^m04^s$ | 14 |

† Each science image has a dimension of **27952** × **2048** pixels for a total observing time of 630 seconds.

Table 2: Characteristics of detected objects†

| No. | SSN | Date (UT) | Time (UT) Pred. | Time (UT) Obs. | $\Delta t$ (s) | $\phi$ (°) Pred. | $\phi$ (°) Obs. | $\Delta\phi$ (°) | $m_G$ | $r$ (km) | $v$ (″/sec) | $d$ (m) $\beta = 1$ | $d$ (m) $\beta = 0.5$ | $\varphi$ (°) | Object type |
|---|---|---|---|---|---|---|---|---|---|---|---|---|---|---|---|
| 1 | 13070 | 2015-05-16 | 20:16:41 | 20:17:21 | 40 | 24.5 | $24.5 \pm 1.0$ | 0.0 | $11.8 \pm 0.1$ | 18423.2 | 30.0 | $2.4 \pm 0.1$ | $2.7 \pm 0.1$ | 54.3 | Payload |
| 2* | 24827 | 2015-05-16 | 23:07:50 | 23:08:30 | 40 | 154.1 | $152.3 \pm 0.6$ | 1.8 | $5.6 \pm 0.2$ | 2525.4 | 507.0 | $7.5 \pm 0.7$ | $7.6 \pm 0.7$ | 81.6 | Payload |
| 3 | 22689 | 2015-05-17 | 21:50:14 | 21:50:42 | 28 | 6.7 | $4.7 \pm 0.1$ | 2.0 | $8.3 \pm 0.1$ | 1411.0 | 1016.0 | $1.1 \pm 0.1$ | $1.2 \pm 0.1$ | 67.5 | Payload |
| 4 | 22488 | 2015-05-17 | 22:15:29 | 22:15:58 | 29 | 7.2 | $4.9 \pm 0.1$ | 2.1 | $6.6 \pm 0.2$ | 991.2 | 1446.8 | $1.7 \pm 0.2$ | $1.8 \pm 0.2$ | 71.8 | Rocket body |
| 5* | 29669 | 2015-05-18 | 16:20:11 | 16:20:30 | 19 | 20.2 | $20.2 \pm 1.1$ | 0.0 | $12.0 \pm 0.3$ | 22516.3 | 22.7 | $2.8 \pm 0.4$ | $3.1 \pm 0.4$ | 59.0 | Rocket body |
| 6 | 32271 | 2015-05-18 | 17:58:57 | 17:59:07 | 14 | 156.4 | $156.3 \pm 0.2$ | 0.1 | $10.5 \pm 0.5$ | 13434.0 | 54.6 | $3.2 \pm 0.8$ | $3.7 \pm 0.8$ | 49.8 | Rocket body |
| 7* | 4367 | 2015-05-19 | 21:05:09 | 21:05:03 | 6 | 12.6 | $14.6 \pm 0.1$ | 2.0 | $6.7 \pm 0.1$ | 1065.4 | 1376.5 | $1.6 \pm 0.1$ | $1.7 \pm 0.1$ | 60.8 | Rocket body |
| 8 | 10539 | 2015-05-19 | 21:42:34 | 21:42:37 | 3 | 168.7 | $167.0 \pm 0.7$ | 1.7 | $7.3 \pm 0.1$ | 1151.0 | 1223.0 | $1.4 \pm 0.1$ | $1.5 \pm 0.1$ | 66.5 | Payload |
| 9* | 17582 | 2015-05-24 | 20:34:52 | 20:35:30 | 38 | 6.9 | $5.6 \pm 0.9$ | 1.3 | $9.3 \pm 0.1$ | 1396.3 | 1027.6 | $1.0 \pm 0.1$ | $1.1 \pm 0.1$ | 57.6 | Payload |
| 10 | 22646 | 2015-05-17 | 16:01:40 | 16:02:01 | 39 | 175.4 | $174.8 \pm 0.1$ | 0.2 | $11.2 \pm 0.5$ | 1401.2 | 1024.4 | $1.1 \pm 0.1$ | $1.3 \pm 0.1$ | 61.4 | Payload |
| 11* | 25770 | 2015-05-18 | 16:31:44 | 16:32:27 | 43 | 140.4 | $137.8 \pm 0.3$ | 2.2 | $7.6 \pm 0.3$ | 2046.0 | 660.4 | $1.9 \pm 0.3$ | $2.2 \pm 0.3$ | 57.5 | Payload |
| 12 | 24827 | 2015-05-19 | 22:36:45 | 22:37:18 | 33 | 154.0 | $152.4 \pm 0.3$ | 1.6 | $6.0 \pm 0.1$ | 2525.6 | 507.0 | $5.7 \pm 0.3$ | $5.9 \pm 0.3$ | 75.8 | Payload |
| 13 | 16759 | 2015-05-17 | 20:30:14 | 20:30:44 | 30 | 166.6 | $164.8 \pm 0.1$ | 1.8 | $8.8 \pm 0.1$ | 1399.5 | 1019.0 | $0.7 \pm 0.1$ | $0.8 \pm 0.1$ | 55.9 | Payload |

† SSN is the catalog number of the object in the database of the US Space Surveillance Network and $\Delta t$ and $\Delta\phi$ are absolute differences between the predicted and observed times and directions, respectively. The remaining symbols are described in the text. Asterisk symbol (*) is assigned to the debris having observed time accuracy of 1 second.

Table 3: Estimated and archived debris cross-sections

| No. | SSN | Optical cross-section ($m^2$) | | Cross-section from DISCOS ($m^2$) | |
|---|---|---|---|---|---|
| | | $\beta = 1$ | $\beta = 0.5$ | min | max |
| 1 | 13070 | 4.5 ± 0.4 | 5.7 ± 0.4 | 1.5 | 13.8 |
| 3 | 22689 | 0.9 ± 0.2 | 1.1 ± 0.2 | 0.5 | 1.4 |
| 4 | 22488 | 2.3 ± 0.5 | 2.5 ± 0.6 | 4.5 | 16.4 |
| 5 | 29669 | 6.2 ± 1.8 | 7.5 ± 1.9 | 5.6 | 10.2 |
| 6 | 32271 | 8.0 ± 4.0 | 10.8 ± 4.6 | 4.2 | 8.7 |
| 7 | 4367 | 2.0 ± 0.3 | 2.3 ± 0.3 | 1.8 | 9.6 |
| 9 | 17582 | 0.8 ± 0.2 | 1.0 ± 0.2 | 0.5 | 1.4 |
| 10 | 22646 | 1.0 ± 0.2 | 1.3 ± 0.2 | 0.5 | 1.4 |
| 11 | 25770 | 2.8 ± 0.9 | 3.8 ± 1.0 | 0.4 | 6.8 |
| 13 | 16759 | 0.4 ± 0.1 | 0.5 ± 0.1 | 0.5 | 0.6 |

Table 4: Upper size limit of the undetected objects[†]

| No. | SSN | Date (UT) | Time (UT) | $r$ (km) | $d_{max}$ (m) | $\varphi$ (°) | Object type |
|---|---|---|---|---|---|---|---|
| 1 | 29904 | 2015-5-16 | 21:54:05 | 868.7 | 0.53 | 67.5 | Satellite debris |
| 2 | 39321 | 2015-5-17 | 21:50:40 | 704.0 | 0.48 | 67.0 | Satellite debris |
| 3 | 18807 | 2015-5-17 | 22:15:13 | 1191.5 | 0.62 | 71.0 | Satellite debris |
| 4 | 37704 | 2015-5-18 | 21:09:02 | 1180.1 | 0.61 | 60.3 | Satellite debris |
| 5 | 30662 | 2015-5-18 | 21:25:57 | 900.4 | 0.54 | 62.9 | Satellite debris |
| 6 | 34683 | 2015-5-18 | 22:18:28 | 735.4 | 0.49 | 71.7 | Satellite debris |
| 7 | 27688 | 2015-5-22 | 21:37:02 | 702.6 | 0.48 | 64.7 | Satellite debris |
| 8 | 23418 | 2015-5-24 | 22:10:49 | 888.3 | 0.54 | 70.0 | Satellite debris |
| 9 | 30079 | 2015-5-24 | 22:41:17 | 896.5 | 0.54 | 75.8 | Satellite debris |
| 10 | 27902 | 2015-5-26 | 19:36:25 | 9068.9 | 1.42 | 47.1 | Satellite debris |

[†] The size information of these objects from online sources is not available.

Table 5: Telescope parameters of DFOT and ILMT

| | DFOT [30, 31] | ILMT [32] |
|---|---|---|
| Primary mirror diameter | 1.31-m | 4.0-m |
| Fraction of reflecting area | 0.69 | 0.95 |
| System efficiency in SDSS $i'$ | 0.42 | 0.63 |

## Appendix A. Optical diameter of a diffuse-specular Lambertian sphere

The phase function, $F(\varphi)$ represents the angular distribution of sunlight intensity scattered by an object at a given wavelength as a function of the phase angle $\varphi$. The phase functions of a diffuse sphere $F_1(\varphi)$ and a specular sphere $F_2(\varphi)$ can be represented as [33],

$$F_1(\varphi) = \frac{2}{3\pi^2}[(\pi - \varphi)\cos\varphi + \sin\varphi] \tag{A.1}$$

$$F_2(\varphi) = \frac{1}{4\pi} \tag{A.2}$$

In the context of the diffuse-specular Lambertian sphere model, the mixing coefficient $\beta$ is used to combine both the phase functions described above and calculate the apparent brightness $m$ of the reflected sunlight from the sphere.

$$m = m_\odot - 2.5\log(A\rho[\beta F_1(\varphi) + (1-\beta)F_2(\varphi)]) + 5\log(r) \tag{A.3}$$

where $A = \pi d^2/4$ is the cross-sectional area of the sphere having a diameter $d$, $m_\odot$ is the apparent magnitude of Sun, $\rho$ is the albedo and $r$ is the range to the object. By replacing the values of $F_1(\varphi)$, $F_2(\varphi)$ and $A$, the expression for the optical diameter of the hybrid model can be written as;

$$d = \frac{r10^{-0.2(m-m_\odot)}}{\sqrt{\rho[\frac{\beta}{6\pi}[\sin\varphi + (\pi-\varphi)\cos\varphi] + \frac{1-\beta}{16}]}} \tag{A.4}$$

Highlights:

- Opportunistic space debris detection using zenith-pointing telescope dedicated to surveys in time-delay-integration mode .
- Efficient image processing and calibration technique.
- Debris identification from the images using two-line element sets.
- Effective optical size estimation from observed flux of the space debris.